nature chemistry

ARTICLES

PUBLISHED ONLINE: 10 OCTOBER 2016 | DOI: 10.1038/NCHEM.2616

A synthetic redox biofilm made from metalloprotein–prion domain chimera nanowires

Lucie Altamura[1,2,3†], Christophe Horvath[1,2,3†], Saravanan Rengaraj[1,2,3,4,5†‡], Anaëlle Rongier[1,2,3,6,7,8], Kamal Elouarzaki[4,5], Chantal Gondran[4,5], Anthony L. B. Maçon[1,2,3‡], Charlotte Vendrely[9,10], Vincent Bouchiat[11], Marc Fontecave[1,2,3,12], Denis Mariolle[13], Patrice Rannou[6,7,8], Alan Le Goff[4,5], Nicolas Duraffourg[1,2,3], Michael Holzinger[4,5*] and Vincent Forge[1,2,3*]

Engineering bioelectronic components and set-ups that mimic natural systems is extremely challenging. Here we report the design of a protein-only redox film inspired by the architecture of bacterial electroactive biofilms. The nanowire scaffold is formed using a chimeric protein that results from the attachment of a prion domain to a rubredoxin (Rd) that acts as an electron carrier. The prion domain self-assembles into stable fibres and provides a suitable arrangement of redox metal centres in Rd to permit electron transport. This results in highly organized films, able to transport electrons over several micrometres through a network of bionanowires. We demonstrate that our bionanowires can be used as electron-transfer mediators to build a bioelectrode for the electrocatalytic oxygen reduction by laccase. This approach opens opportunities for the engineering of protein-only electron mediators (with tunable redox potentials and optimized interactions with enzymes) and applications in the field of protein-only bioelectrodes.

Electron transport through proteins is a central mechanism of life involved in the storage and use of energy in many biological processes. For instance, photosynthesis requires long-range electron transport to convert solar energy into chemical energy. Electron transfers are also involved in redox enzymes that catalyse essential biosynthetic and metabolic reactions in all living organisms. Proteins are the key players as they allow both intra- and intermolecular electron shuttling.

It is therefore very tempting to draw on natural systems for engineering artificial bioelectronic systems. For example, the discovery of natural biofilms able to transport electrons efficiently over long distances has attracted a great deal of interest[1–3]. These biofilms are made of a network of conductive nanowires that connect bacteria to each other or to metal oxides present in their environment. However, both their self-assembly processes and their structural organization have not been unravelled fully. Although the electron-transport mechanism within these bionanowires is not fully understood[4–7], it is generally assumed that electron hopping between redox centres is central for the conductivity of biofilms[8].

For our design, we took inspiration from the architecture of these biofilms, namely a network of electrochemically active nanowires composed of a redox protein aligned onto a filament. This can be considered as a biomimetic 'bottom-up' design of redox films. Domains that form amyloid fibres, sometimes called prion domains, are good candidates for nanotechnologies based on protein self-assembly[9–11]. Metallic conductivity can be provided by fibre metallization[12] and semiconducting behaviours can result from the intrinsic properties of self-assembled fibres given by π-stacked aromatics or charged groups at their surfaces[13–19]. They can also be incorporated into hybrid devices with luminescent or shape-memory properties[20–23]. Furthermore, it has been shown that it is possible to unfold and refold a protein bound on the surface of an amyloid fibre[24].

Here we report the design of conductive protein bionanowires by coupling a self-assembling prion domain and a redox protein within a chimeric protein. Self-assembly of the fibre is driven by the prion domain, which thus allows a spatially controlled arrangement of the redox protein along the fibre. The chosen prion domain derives from a prion protein, HET-s, found in the filamentous fungus *Podospora anserina* and involved in self/non-self recognition processes through heterokaryon incompatibility[25]. This protein displays two distinct domains: an N-terminal recognition domain followed by a C-terminal (HET-s(218-289)) prion to form domain PFD(HET-s)[26] (PFD, prion-forming domain). The structure of the fibrils made from PFD(HET-s) has been solved by solid-state nuclear magnetic resonance (ssNMR) and corresponds to a β-solenoid with a triangular hydrophobic core[27]. Each prion domain covers two turns of the solenoid, which represents a step of 0.94 nm.

The two HET-s domains are structurally and functionally independent. Therefore, we could generate a chimeric protein, named Rd-HET-s(218-289), in which the N-terminal domain was replaced by rubredoxin (Rd), a redox protein, without altering the ability of PFD(HET-s) to form fibrils. Rd was selected because it is a natural electron-carrier metalloprotein in biological systems[28]. Its active site contains a $Fe^{2+/3+}$ iron centre, chelated by four cysteines in a tetrahedral

[1]Université Grenoble Alpes, BIG-LCBM, F-38000 Grenoble, France. [2]CNRS, BIG-LCBM, F-38000 Grenoble, France. [3]CEA, BIG-LCBM, F-38000 Grenoble, France. [4]Université Grenoble Alpes, DCM UMR 5250, F-38000 Grenoble, France. [5]CNRS, DCM UMR 5250, F-38000 Grenoble, France. [6]Université Grenoble Alpes, INAC-SPrAM, F-38000 Grenoble, France. [7]CNRS, INAC-SPrAM, F-38000 Grenoble, France. [8]CEA, INAC-SPrAM, F-38000 Grenoble, France. [9]ERRMECe, I-MAT FD4122, Université de Cergy-Pontoise, 2 avenue Adolphe Chauvin, 95302 Cergy-Pontoise Cedex, France. [10]LMGP, CNRS UMR 5628, 3 parvis Louis Néel, 38016 Grenoble, France. [11]Institut Néel, CNRS-UJF-INP, 38042 Grenoble Cedex 09, France. [12]Laboratoire de Chimie des Processus Biologiques, UMR 8229 CNRS, Université Pierre et Marie Curie – Paris 6, Collège de France. 11 Place Marcelin Berthelot, 75231 Paris Cedex 05, France. [13]CEA, LETI, MINATEC Campus, F-38054 Grenoble, France. †These authors contributed equally to this work. ‡Present addresses: Department of Chemical Engineering, University of Bath, Bath BA2 7AY, UK (S.R.); Nagoya Institute of Technology, Frontier Research Institute, Nagoya, Aichi 466-8555, Japan (A.L.B.M.). *e-mail: michael.holzinger@univ-grenoble-alpes.fr; vincent.forge@cea.fr

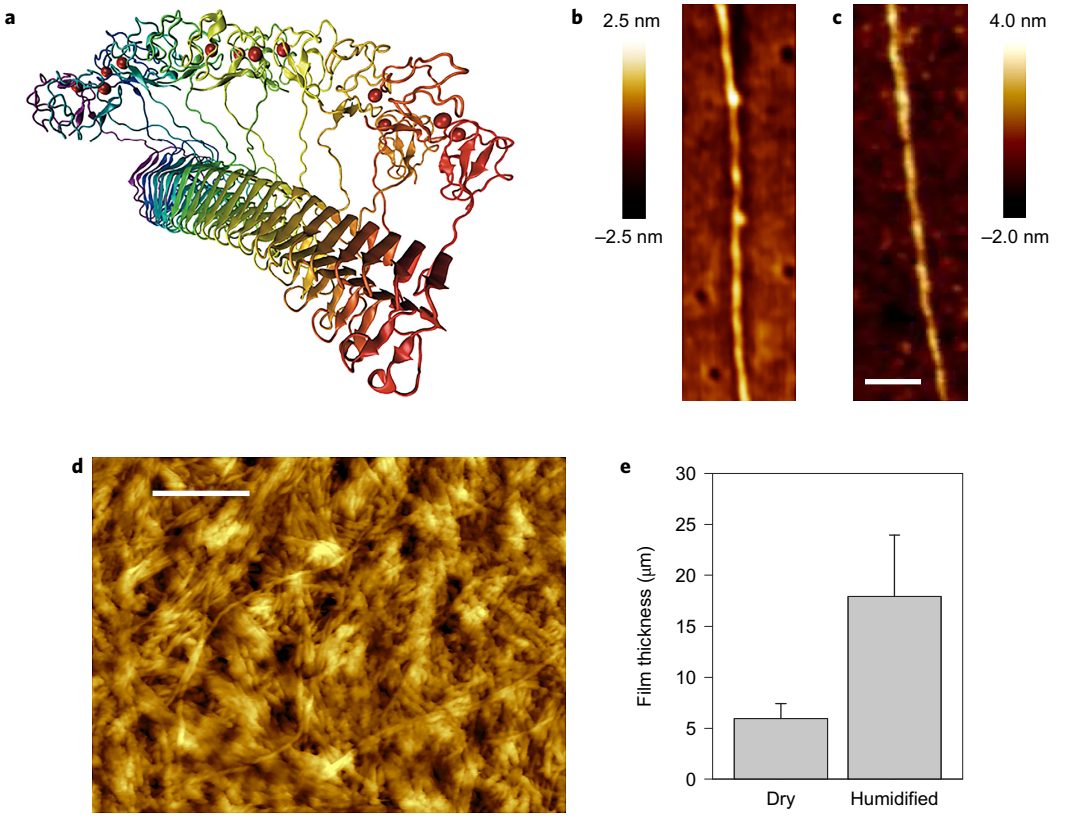

Figure 1 | Structural features of Rd-HET nanowires and redox film. a, The structural model of Rd-HET nanowires shows a side view of twelve Rd-HET-s(218-289) molecules within an amyloid fibre, with the iron atoms represented as large red dots. Each molecule is coloured uniquely. The building of this model, which represents the expected structure of Rd-HET nanowires, is described in Methods. **b**,**c**, AFM images of fibrils obtained at pH 4.5, made of either PFD(HET-s) only (**b**) or Rd-HET-s(218-289) (**c**). Scale bar, 50 nm. **d**, Peak-force tapping AFM image of the nanowire film used for electrochemistry, that is, on drying of the acidic gel droplet and the electrode dropped into the PPB at pH 7.4. The image was recorded before the film drying. Scale bar, 200 nm. **e**, Film thickness measured by confocal scanning microscopy on the film, either in the dry state or on hydration. Error bars represent the standard deviation obtained from the thickness measurement of three different films.

configuration. Rd from *Methanococcus voltae* was chosen because it is one the smallest members of the Rd family (44 residues, 5.2 kDa).

The charge transfers within bionanowire films by electron hopping between reduced and oxidized Rd linked to self-assembled prion domains were evidenced by cyclic voltammetry (CV) and electrochemical impedance spectroscopy (EIS). Subsequently, these novel bioinspired conductive films were exploited as mediators for enzyme wiring and electron shuttling to electrodes. More specifically, an efficient electron transfer was demonstrated with the multicopper enzyme laccase involved in bioelectrocatalytic oxygen reduction processes[29]. Such enzyme-wiring capacities combined with the intrinsic electrical conductivity of these bionanowires open vast possibilities for bioelectronics.

Results and discussion

Nanowire design and self-assembly. *Rd* and *HET-s(218-289)* genes were fused into a synthetic plasmid which was transformed into *E. coli* and induced for expression of the chimeric protein[26]. The overexpressed protein was then extracted and purified. The resulting chimeric protein, Rd-HET-s(218-289), has a sequence 123 amino acids long and a molecular weight of 13.8 kDa (Supplementary Fig. 1). The expected structure of the bionanowires is illustrated in Fig. 1a. It shows 12 subunits of Rd-HET-s(218-289) assembled into a nanowire, named Rd-HET hereafter. Such a representation of the protein is based on the structure of PFD(HET-s) determined by ssNMR[27,30], and on that of a Rd obtained by X-ray diffraction[31]. The Rds and their iron centres are helically aligned around the fibre generated by the self-assembly of the prion domains. Figure 1a shows a favourable conformation with distances between the iron centres of about 1 nm, that is, similar to the size of the prion domain and thus clearly less than 25 Å, the limit for an electron transfer[32,33]. It is obvious, however, that the linker between the two folded domains, which corresponds to the unfolded N-terminal part of HET-s (218-289), allows some mobility of the redox domains on the fibres. This implies some dynamics of the redox domains, with some effects on the charge transfers.

As for the wild-type PFD(HET-s), the morphology of the fibres derived from the chimeric protein depends on the pH of the solution[34]. Isolated fibrils were formed at low pH (below pH 5), as shown in the transmission electron microscope image (Supplementary Fig. 2). At neutral pH, the fibrils were associated into thick bundles (Supplementary Fig. 2). In the case of the wild-type prion domain, the apparent diameter of the elementary fibrils was about 6 nm, for an average length of 12 μm (ref. 35), whereas the bundle diameter varied from 100 to 200 nm (refs 34,36). The isolated fibres formed from Rd-HET-s(218-289) at pH 4.5 had an apparent diameter of ~8 nm, whereas the bundles obtained at pH 7.5 showed diameters larger than 100 nm. At the macroscopic scale, the isolated fibrils at an acidic pH, called singlet fibrils, formed a homogeneous gel, whereas the bundles at neutral pH had the tendency to form sedimenting knots.

Singlet fibrils at acidic pH from PFD(HET-s) (Fig. 1b) and from Rd-HET-s(218-289) (Fig. 1c) were also characterized by atomic force microscopy (AFM). In both cases, a left-handed twist was observed with a pitch of ~39 ± 7 nm, in agreement with the value

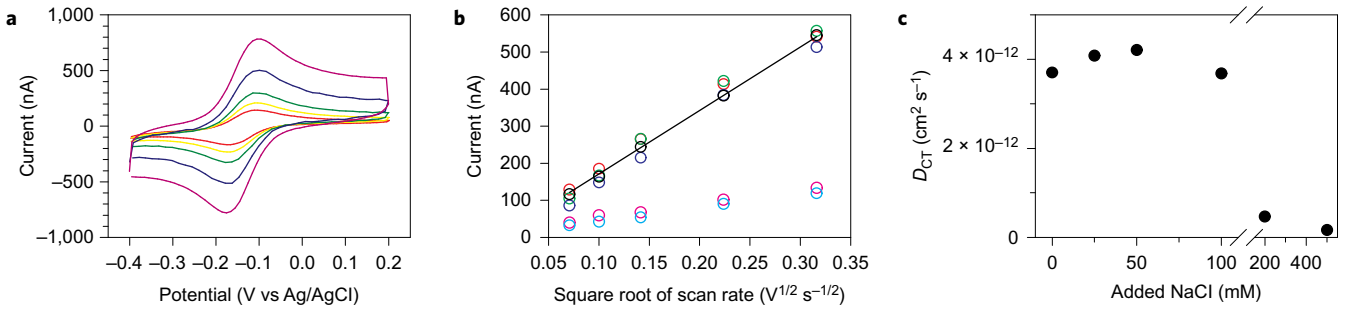

Figure 2 | Electrochemistry of Rd-HET redox film. a, CV of a Rd-HET 'thick' film over a GCE in 0.1 M PPB, at pH 7.4. Scan rates are 5 (red), 10 (yellow), 20 (green), 50 (blue) and 100 (purple) mV s^{-1}. **b**, Scan-rate dependency study of peak current at different electrolyte concentrations. Peak currents correspond to the redox peak height on subtracting the capacitive component, which increases also with the scan rate. Anodic current (oxidation) without added NaCl (black circles); with added 25 mM NaCl (red circles), 50 mM NaCl (green circles), 100 mM NaCl (blue circles), 200 mM NaCl (purple circles) and 500 mM NaCl (cyan circles). The continuous line corresponds to the linear regression on the data obtained in the absence of added NaCl. **c**, Plot of D_{CT} and the electrolyte concentration. The D_{CT} values were extracted from scan-rate dependencies at different NaCl concentrations.

derived from cryoelectron microscopy[37]. The presence of Rd on the fibrils had no significant effect on the observed heights; the Rd domains were most probably swept by the tip because of the flexibility of the linker between the two domains (Fig. 1a). This resulted in an apparent lower resolution of the fibril edges (Fig. 1b,c).

Electrochemistry of Rd-HET redox films. The spectroscopic (ultraviolet–visible light and electron paramagnetic resonance spectroscopy) properties of Rd on the surface of Rd-HET bionanowires were similar to those of Rd free in solution (Supplementary Fig. 3). According to the electrochemical measurements (Supplementary Fig. 3), the redox properties of Rd on the nanowires were not altered either; the redox potential $E_{1/2}$, which corresponds to the reversible monoelectronic $Fe^{2+/3+}$ system of Rd, was −0.12 V vs Ag/AgCl for both Rd alone and Rd-HET.

Electrochemical experiments were carried out to verify whether Rd-HET could facilitate electron transfer at the interface of the electrode surface (surface-confined electron-transfer process) and electron diffusion through Rd-HET films (diffusional electron-transfer process). To elucidate the electron-transfer process, two types of Rd-HET films, thin and thick films, were deposited at pH 4 onto a glassy carbon electrode (GCE). For the thin film, the fibre adsorption on the GCE was allowed for 30 minutes. The electrode was then rinsed with water to remove the unbound fibres and keep only the fibres in a tight interaction. These so-called thin films had a thickness of ~1.3 µm (Supplementary Fig. 4), which was much more than expected for a protein monolayer. Owing to the high aspect ratio (a diameter of ~5 nm for an average length of 12 µm) and the flexibility of the bionanowires, the layer formed this way was more probably an intricate network than a real monolayer. The exact nature of the interaction between the fibres and the GCE is still under investigation. However, favourable electrostatic interactions between the negatively charged GCE electrode and the positively charged proteins at pH 4.5 (isoelectric point $(pI)_{(Rd\text{-}HET)} = 7.7$) are likely to play a role. CV was used to investigate these bioelectrodes in a potassium phosphate buffer (PPB) at neutral pH (Supplementary Fig. 4). The redox wave at $E_{1/2ox} = -0.12$ V vs Ag/AgCl had a peak-to-peak separation (ΔEp) of 2 mV, close to the theoretical value of 0 mV expected for a surface-confined electron-transfer process. The linear dependence of the peak currents as a function of the scan rate revealed a fast and efficient electron transfer from the electrode to the first bionanowire layers (Supplementary Fig. 4). Thus, the electron-exchange rate between the Rd-HET thin film and the electrode was not limited by diffusion processes within this range of scan rates. A surface coverage of $\Gamma = 6.2 \times 10^{-11}$ mol cm^{-2} for Rd-HET monomers was estimated by the integration of the charge of the redox peaks at slow scan rates.

Owing to the protocol used for its preparation, the thick film was a dense and intricate network of both short bundles and isolated fibrils, as confirmed by peak-force tapping AFM (Fig. 1d). First, when still singlet fibrils the bionanowires were drop cast onto a GCE at pH 4 as a homogeneous gel; they were then left to dry. For the electrochemistry experiment, the electrode was dipped into a PPB at neutral pH. At this pH, the bionanowires have the tendency to assemble and form bundles (Supplementary Fig. 2). However, as a result of their high concentration on the electrode surface before the pH jump from pH 4 to pH 7.4, the nanowires do not have the ability to reorganize themselves into long bundles. Instead, short bundles that involve short sections of bionanowires, are formed. They are a few hundreds of nanometres long (Fig. 1d), whereas the bundles formed at low concentrations are tens of micrometres long (not shown). The obtained architecture is illustrated in Supplementary Fig. 6, and results in the formation of a hydrogel that stabilizes the film on the electrode surface and keeps some softness. Indeed, whereas the 'dry film' was 6 µm thick, after humidification of the Rd-HET film a thickness of 18 µm was measured (Fig. 1e and Supplementary Fig. 5). This swelling effect is consistent with that already observed in redox hydrogel films[38]. Furthermore, the Rd-HET film showed a remarkable stability over time—CVs recorded periodically over six days showed a signal loss of only ~20% (Supplementary Fig. 7). As control experiments, we observed that functionalized electrodes using adsorbed Rd as well as mixtures of PFD(HET) and Rd (Supplementary Fig. 7) exhibited only low-intensity redox signals, probably because of the rapid release of Rd in solution. No redox signal was detected when PFD(HET) was used alone.

For thick Rd-HET films, ΔEp was equal to 62 mV, close to the theoretical value of 56.4 mV, as expected at a low scanning rate for a reversible monoelectronic diffusion-controlled redox system (Fig. 2a). At increasing scan rates, the peak current linearly increased with the square root of the scan rate (Fig. 2b). Such behaviour indicates that the electron transfer within the protein nanowire film was governed by linear diffusion[39]. Using the Randles–Sevcik equation, an apparent charge-transport diffusion coefficient (D_{CT}) of $(3.7 \pm 0.5) \times 10^{-12}$ cm^2 s^{-1} was estimated from the slope of the linear dependency shown in Fig. 2b, taking into account a film thickness of 18 µm. The swelling effect indicated that the solvent could penetrate the film. Therefore, the ions (protons, Na^+, Cl^-, …) could diffuse within the film and thus contribute to the charge transport. The same experiment was repeated for different electrolyte concentrations between 0.025 and 0.5 M. Up to 0.1 M of NaCl, no significant change of both the CVs and the peak-current dependencies on the scan rate could be observed (Fig. 3b and Supplementary Fig. 8). For electrolyte concentrations above 0.1 M,

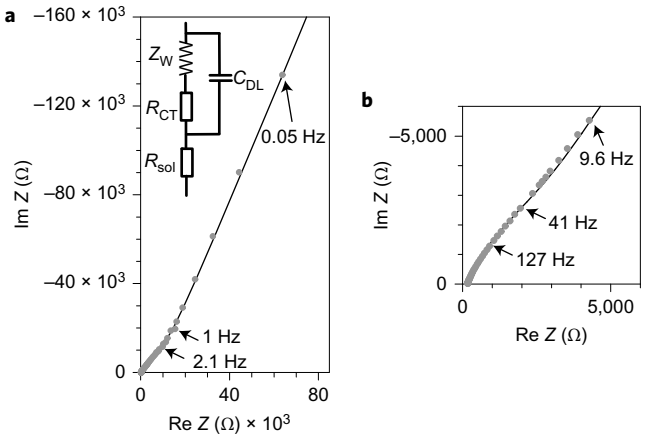

Figure 3 | EIS on Rd-HET redox film. a, Nyquist plot of impedance spectra of Rd-HET drop cast on a GCE in 0.1 M phosphate buffer (pH 7.4). Inset, equivalent circuit used to fit the experimental data. **b**, Zoom at the high-frequency impedance range. The frequency sweep was from 50 kHz to 0.05 Hz. Impedance measurements were performed at −0.12 V vs Ag/AgCl with an a.c. amplitude of 10 mV. Experimental (dots) and fitted data (lines) are presented.

the current intensity in the CV decreased because of film damage as a result of nanowire aggregation at high ionic strength (data not shown). For the different electrolyte concentrations, D_{CT} was estimated based on the peak current versus scan-rate dependencies and from the redox protein concentration within the film (Fig. 2c). It remained quite constant for electrolyte concentrations up to 0.1 M. Moreover, CVs recorded on the same film at different pH values (from 4.5 to 7.4) were basically the same (Supplementary Fig. 8). Therefore, current and the associated D_{CT} values depend on neither the ionic strength nor the pH, which demonstrates that the charge transfer monitored by electrochemistry within the films was not controlled by ionic or proton diffusion. Nevertheless, to preserve the electroneutrality the diffusion of ions and protons within the film was probably important to compensate the charge (electron) transfers. Therefore, the charge transfer within the thick film was determined by electron transfers between the Rd units via a hopping mechanism. Furthermore, the alignment of the redox centres along the fibres was essential to obtain a fully reversible electroactive film. In fact, when the GCE was functionalized with PFD(HET) and Rd crosslinked using glutaraldehyde vapours, the redox system was poorly reversible with a ΔEp of 300 mV (Supplementary Fig. 9). These control experiments further highlighted the unique redox properties of the Rd-HET bionanowires compared with those of disordered redox protein films.

The association of Rd with a prion domain thus allowed the formation of a stable biofilm that kept the local concentration of Rd on the electrode surface high enough to have a good electrochemical signal. Furthermore, it induced the organization of a dense network of Rd, that is, close enough to each other to allow for an efficient electron transport between Fe centres throughout dozens of micrometres, most probably by an electron-hopping mechanism. Such formalism has been applied to describe electron hopping within self-assembled redox polymers[40–42]. For comparison, redox polymers based on ferrocene or osmium complexes attached to a polymer backbone exhibit D_{CT} coefficient values that range from 10^{-6} to 10^{-12} cm^2 s^{-1} (ref. 38). A diffusion coefficient for Rd-HET films in the lower limit might result in the larger protein–protein distance as well as in a lower redox-centre mobility as compared with small redox molecules involved in these redox polymers.

EIS[43] allows an insight into the redox phenomena that occurs within electroactive films made of redox polymers[44,45]. The same three-electrode set-up as used to record CVs was used; the overpotential was fixed at the redox potential of Rd (−0.12 V vs Ag/AgCl) and small-amplitude oscillations of various frequencies were applied. Therefore, only the impedance caused by the redox phenomenon was monitored in this experiment. The Nyquist plot from the EIS measurements for the modified electrode fitted perfectly the equivalent circuit model displayed at the top of Fig. 3. This model comprised two resistance elements: R_{sol} for the ohmic resistance of the electrolyte solution and R_{CT} for the charge-transfer resistance between the film and the GCE. One double-layer capacitance (C_{DL}) and a Warburg impedance Z_W element for the linear electron diffusion within the electroactive film completed the circuit[44–47]. The value of R_{sol} corresponded to the impedance where the Nyquist plot crossed the 'Re Z' axis at high frequencies (Fig. 3, inset), $R_{sol} = 11.5 \pm 0.5\ \Omega\ cm^2$. The high-frequency semicircle of the Nyquist diagram (Fig. 3b, below 41 Hz) corresponded to the charge-transfer resistance in parallel to the double-layer capacitance, $R_{CT} = 450 \pm 20\ \Omega\ cm^2$ and $C_{DL} = 14.8 \pm 0.5\ \mu F\ cm^{-2}$. At low frequencies (Fig. 3a, between 9.6 and 0.05 Hz), two successive linear parts were observed. The linear part for frequencies above 1 Hz had a slope close to one, whereas that between 1 and 0.05 Hz was almost vertical. Such a broken slope is characteristic of a restricted finite-length diffusion process of the diffusing redox species[44–47]. Between 9.6 and 1 Hz, the impedance adopted the form of a characteristic Warburg element with a slope of one in the complex impedance plane, $Z_W = 560 \pm 20\ \Omega\ cm^2$. When the modulation frequency was lower, the impedance described a 'blocking' surface, which means that the redox species were confined within the electroactive film[44–47]. In our case, the only way to explain such a phenomenon is via an electron-hopping mechanism between the Fe^{2+}/Fe^{3+} redox centres of the nanowires within the film. The contribution of proton or ionic diffusion to the charge-transport impedance (Z_W) can be excluded. Indeed, protons and ions could freely diffuse between the bulk and the film. Thus, if their diffusion could control the charge-transport impedance, a completely different behaviour would be observed in the Nyquist plot[43,46,48], that is, a semi-infinite diffusion or finite-length diffusion with transmissive boundary conditions. In the case that their diffusion constant would not be modified between the bulk and the film, the slope of the Nyquist plot would remain close to 1 as expected for a semi-infinite process[43,46]. In the case that a concentration gradient would appear within the electroactive film because their diffusion constant would become slower due to the local viscosity, the Nyquist plot should follow a semi-circle at low frequencies, as expected for a transmissive finite-length diffusion process[43,48]. In the ideal case, the slope of the Nyquist plot at low frequency should be vertical (with an angle of 90°) for a restricted finite-length diffusion process[44–48]. That the angle we observed was smaller than 90° reflected some inhomogeneity in the electroactive film thickness[45,48], that is, the roughness of the interface, as could be seen by confocal microscopy (Supplementary Fig. 5). The way that the interface inhomogeneity was taken into account for the fitting to the electric circuit is explained in Methods.

Furthermore, these features enabled the identification of two successive phenomena that governed, in equal parts, the electrochemical kinetics: electron transfer at the interface Rd-HET/electrode, $R_{CT} = 450 \pm 20\ \Omega\ cm^2$, and the diffusion of electrons inside the Rd-HET film, $Z_W = 560 \pm 20\ \Omega\ cm^2$. Considering a thickness of 18 μm and an electrode diameter of 3 mm, it was possible to estimate from the Z_W value the electrical conductivity of the film to be 3.1 μS cm^{-1}.

The conductivity of protein films in the dry state has already been investigated, in particular for amyloid fibrils[14,16–19,49]. The dominant charge-transport mechanism has been attributed to protonic conductivity[14,49] and the organization of the proteins into fibrils increased the conductivity by several orders of magnitude[14]. It was

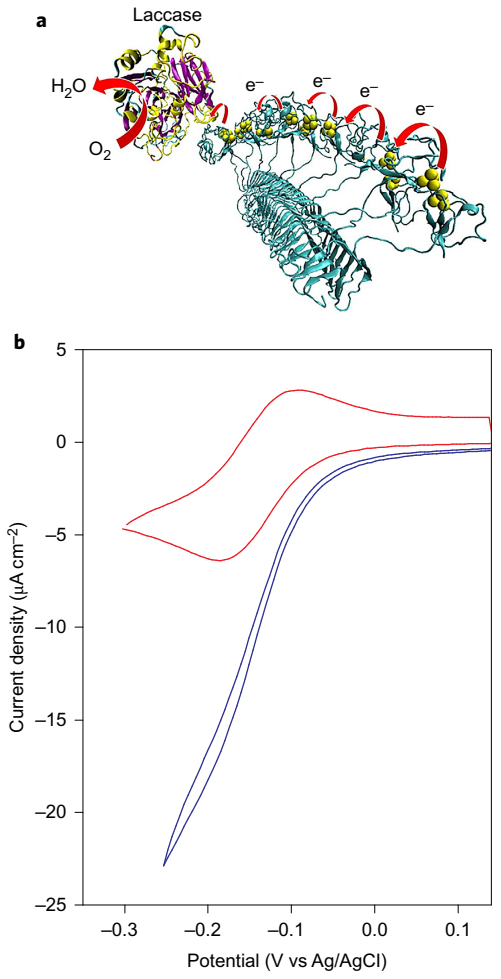

Figure 4 | Rd-HET as a redox mediator for the bioelectrocatalytic reduction of oxygen by laccase. a, Graphical depiction of the electron transfer from the electrode towards laccase through Rd-HET bionanowires. **b**, CV of electrocatalytic-mediated oxygen reduction of Rd-HET/laccase in sodium phosphate buffer (pH 5) at 37 °C. Both the redox couple of Rd-HET-s(218-289)/laccase in deoxygenated sodium phosphate buffer (red line) and the catalytic oxygen reduction of Rd-HET/laccase in the presence of oxygen (blue line) are shown.

interesting to check whether the observed electron-hopping mechanism in the present nanowires caused by a redox process in solution might result in an additional conductivity mechanism in the dry state. For that purpose, current–voltage (I–V) measurements were performed on dried thick films made of either PFD(HET) alone or Rd-HET (Supplementary Fig. 10). Some conductivity was observed for fibres made of PFD(HET) alone, probably caused by protonic and, to some extent, ionic conductivity. However, the I–V curve showed higher current values for Rd-HET and thus a lower resistance value of 50 MΩ as compared with the 143 MΩ for PFD(HET). This suggested that the possibility to have electron hopping provided an additional conductivity to the fibres. However, this remains to be confirmed. From these data, it was possible to estimate the electrical d.c. conductivity of the Rd-HET film to be 2.4 μS cm^{-1}. Both types of a.c. and d.c. conductivity measurements (EIS and I–V, respectively) thus gave consistent values of a few microsiemens per centimetre, which are similar to those reported for natural biofilms made of microbial nanowire networks[50].

Application of Rd-HET nanowires for enzyme wiring. Encouraged by the efficient electron transport of the Rd-HET redox films, we evaluated their ability to connect electrically the soluble redox enzymes to electrodes. As a proof-of-concept, Rd-HET was used as a redox mediator for the bioelectrocatalytic reduction of oxygen by laccase from *Trametes versicolor*. Laccase is a redox enzyme with four redox-active $Cu^{+/2+}$ sites. A Type 1 (T1) copper centre accepts electrons from specific natural partners (phenolic compounds). It can also reduce oxygen electrochemically via crosslinking the enzyme to a redox polymer on the electrode surface[51] or by clamping the enzyme together with carbon nanotubes between permeable membranes and the electrode[52]. More recently, a complex electroactive architecture was proposed with laccase embedded together with cytochrome *c* within a silica-nanoparticle matrix[53,54]. The reduced T1 centre then transferred electrons to the three Type 2/Type 3 (T2/3) copper centres in which molecular oxygen was reduced to water[29]. As the redox potential of the T1 copper centre is $E^{0'}$ = +0.585 V vs Ag/AgCl, and thus much higher than that of Rd (−0.12 V vs Ag/AgCl), electron transfer between Rd and laccase possesses a large driving force. Furthermore, electrostatic interactions favour the association of the positively charged Rd-HET (pI = 7.7) and the negatively charged laccase (pI = 3.5), and minimize the distance between the redox centres, which thus facilitates interprotein electron transfer[55,56]. Figure 4 shows the electrocatalytic reduction of oxygen by laccase mediated by Rd-HET nanowires using CV. For this experiment, laccase and Rd-HET fibres were drop cast onto GCE and crosslinked after drying. Then, CVs were recorded either in the absence or in the presence of oxygen. In the absence of oxygen (Fig. 4, red line), only the redox signal caused by the monoelectronic $Fe^{2+/3+}$ system of Rd was observed. In the presence of oxygen (Fig. 4, blue line), a catalytic reduction wave was observed, starting at the foot of the redox signal of Rd, that is, at $E^{0'} \approx -0.05$ V. Chronoamperometric measurements performed at $Ep = -0.25$ V showed the bioelectrocatalytic oxygen-reduction current under operational conditions (Supplementary Fig. 11). The catalytic current in the chronoamperometry correlated closely to the current detected with CV at the same applied potential. Thus, chronoamperometry also confirmed the mediated electrocatalysis for oxygen reduction based on the applied potential. This demonstrates the ability of our bionanowires to shuttle electrons from the electrode to the T1 copper centre[56]. Control experiments (data not shown) using bare glassy carbon or laccase with Rd crosslinked to a film made of the prion domain alone gave no electrocatalytic response. Although weaker than those usually observed with osmium-based redox polymers[51], the current densities using Rd-HET were larger than those reported for electroactive architectures with cytochrome *c* as an electron mediator[53,54]. Additionally the mediators reported here were exclusively made of proteins, very likely to be less toxic than osmium complexes or carbon nanotubes, and thus more suitable for their use within implantable bioelectrode devices.

Conclusions

In conclusion, the original conductive films made of protein nanowires could be produced via the self-assembly of bioengineered proteins. Electrochemical methods, such as CV and EIS, supported an electron-hopping mechanism within and between these wires. The advanced technology proposed here was based on the construction of two-domain proteins, of which one domain contributed to the formation of fibres and the other one to electron transport. As a proof of concept, such protein bionanowires were successfully applied to mediate the electron transfer to the redox enzyme laccase for catalytic oxygen reduction. Using this technique, engineering of a large variety of conductive and other functional bionanowires with tunable compositions and structures is accessible. For instance, Rd can easily be exchanged with other redox proteins to tune the conductivity or to mediate electron transfer for electrocatalytic reactions at

optimal overpotentials. This flexibility opens up many potential applications based on pure protein bio(nano)electronics. Within biomedical devices, for instance, pure protein biosensors powered by pure protein biofuel cells in living organisms that harvest the needed energy directly from the organism (for example, glucose) can be anticipated[57,58].

Methods

The plasmid construct and the expression and purification of the different proteins used in this work are described in the Supplementary Information, together with the various biophysical methods needed for their structural characterization.

Model of the Rd-HET nanowire (Fig. 1a). For the amyloid fibre structure, the ssNMR structure of PFD(HET) (Protein Data Bank (PDB) entry 2RNM) was used. The *M. voltae* Rd structure was generated by analogy with that of *Pyrococcus abyssi* Rd (PDB entry 1YK5) with MODELLER and refined with the CHARMM force field in implicit solvent. The chimeric protein structure was obtained by fusing the two structures with MODELLER and slightly refined with CHARMM. The picture was generated with VMD (Illinois University).

AFM. Fibrils were diluted to a final concentration of 0.28 μM in HCl 0.1 mM and left to adsorb overnight at 4 °C on glass slides cleaned with plasma O_2. After removal of the solution, the samples were left to dry. Images were recorded at a scanning speed of 0.5 Hz in the tapping mode in air with a Dimension 3100 (Bruker) using Si_3N_4 cantilevers of a spring constant of 0.4 N m^{-1}, and were analysed using Nanoscope (Bruker). PeakForce Tapping AFM analysis of the thick film was performed on Dimension ICON (Bruker). ScanAsyst Air tip (Bruker) with a spring constant of 0.35 N m^{-1}, as determined by the thermal tune method, was used. The used PeakForce Setpoint value was 150 pN.

Electrochemistry. CV was performed using a Biologic potentiostat PS200. A three-electrode electrochemical cell with a working volume of 10 ml was used. The working electrode was a GCE (diameter, 3 mm) purchased from Biologic. The reference and counter electrodes were Ag/AgCl and platinum, respectively. To prepare the film, 30 μl of Rd-HET (390 μM) was drop cast onto a GCE and allowed to dry overnight before performing the electrochemical characterizations.

The surface coverages of redox-active species confined to the electrodes were quantified using equation (1).

$$T = Q/nFA \quad (1)$$

where Q is the faradaic charge transferred across the film[39] (determined by integration of anodic peaks of the cyclic voltammogram at low scanning rates (1 mV s^{-1})), n is the number of electrons (that is, $n = 1$) and A (cm^2) is the electrode surface area given a diameter of 3 mm.

The apparent charge transport, D_{CT}, was obtained using the Randles–Sevcik equation (2):

$$i_p = 269{,}000n^{3/2}AD_{CT}^{1/2}Cv^{1/2} \quad (2)$$

where i_p (A) is the maximum current on background subtraction, C (mol cm^{-1}) is the protein concentration and v (V s^{-1}) is the scan rate. The protein concentration within the film was estimated by taking into account the amount of proteins present within the deposited drop and the volume of the film on hydration. Then, D_{CT} was estimated from the slope of the linear dependency of i_p with $v^{1/2}$ (Fig. 2b).

For the electrocatalytic reduction of oxygen, 10 μl of Rd-HET (720 μM) and 5 μl of laccase (*T. versicolor*) at 5 mg ml^{-1} (stock solution prepared in sodium phosphate buffer at pH 5) were drop cast onto a GCE and dried overnight. The pI for Rd-HET was estimated from the amino acid sequence with ExPASy. The electrode was exposed to glutaraldehyde vapour for ten minutes to crosslink Rd-HET and laccase. Experiments were initiated one hour later. The experiments were performed in sodium phosphate buffer at pH 5 (laccase is active at acidic pH) in the presence and absence of oxygen at 37 °C.

a.c. conductivity characterizations performed by EIS. The frequency sweep was from 50 kHz to 0.05 Hz with an a.c. amplitude of 10 mV. The CVs were performed before the EIS measurements. The bias potential applied during the impedance measurement was calculated by $(E_{p,a} + E_{p,c})/2$, where $E_{p,a}$ and $E_{p,c}$ were the anodic and cathodic peak potentials obtained from the CV. The data were fitted with the ZView software (Scribner Associates Inc.) by using an appropriate equivalent electrical circuit model. The equivalent circuit used constant phase elements (CPEs) instead of capacitances to account for imperfections of the electrochemical interface caused by surface inhomogeneity on the modified electrode[59]. The impedance of a CPE is given by:

$$Z_{CPE} = Q^{-1}(j\omega)^{-\alpha}$$

where Q is the amplitude of the CPE, ω is the angular frequency and α is an exponent that is a real number and varies between 0 and 1. When $\alpha = 1$, a purely capacitive behaviour is observed (that is, $Q = C$).

All the experiments were conducted in an anaerobic glovebox to prevent the action of oxygen at room temperature (20 ± 1 °C). For the mediated electron transfer of catalytic oxygen reduction, experiments were conducted outside the glovebox under ambient air at 37 °C.

Received 22 July 2015; accepted 16 August 2016; published online 10 October 2016

References

1. Malvankar, N. S. & Lovley, D. R. Microbial nanowires: a new paradigm for biological electron transfer and bioelectronics. *ChemSusChem* **5,** 1039–1046 (2012).
2. Qian, F. & Li, Y. Biomaterials: a natural source of nanowires. *Nat. Nanotechnol.* **6,** 538–539 (2011).
3. Pfeffer, C. *et al.* Filamentous bacteria transport electrons over centimetre distances. *Nature* **491,** 218–221 (2012).
4. Reardon, P. N. & Mueller, K. T. Structure of the type IVa major pilin from the electrically conductive bacterial nanowires of *Geobacter sulfurreducens*. *J. Biol. Chem.* **288,** 29260–29266 (2013).
5. Malvankar, N. S., Tuominen, M. T. & Lovley, D. R. Lack of cytochrome involvement in long-range electron transport through conductive biofilms and nanowires of *Geobacter sulfurreducens*. *Energy Environ. Sci.* **5,** 8651–8659 (2012).
6. Malvankar, N. S., Tuominen, M. T. & Lovley, D. R. Comment on 'On electrical conductivity of microbial nanowires and biofilms'. *Energy Environ. Sci.* **5,** 6247–6249 (2012).
7. Bonanni, P. S., Massazza, D. & Busalmen, J. P. Stepping stones in the electron transport from cells to electrodes in *Geobacter sulfurreducens* biofilms. *Phys. Chem. Chem. Phys.* **15,** 10300–10306 (2013).
8. Strycharz-Glaven, S. M., Snider, R. M., Guiseppi-Elie, A. & Tender, L. M. On the electrical conductivity of microbial nanowires and biofilms. *Energy Environ. Sci.* **4,** 4366–4379 (2011).
9. Knowles, T. P. J. & Buehler, M. J. Nanomechanics of functional and pathological amyloid materials. *Nat. Nanotechnol.* **6,** 469–479 (2011).
10. Mankar, S., Anoop, A., Sen, S. & Maji, S. K. Nanomaterials: amyloids reflect their brighter side. *Nano Rev.* **2,** 6032–6043 (2011).
11. Gras, S. L. in *Advances in Chemical Engineering* Vol. 35 (ed. Rudy, J. K.) 161–209 (Academic, 2009).
12. Scheibel, T. *et al.* Conducting nanowires built by controlled self-assembly of amyloid fibers and selective metal deposition. *Proc. Natl Acad. Sci. USA* **100,** 4527–4532 (2003).
13. Kholkin, A., Amdursky, N., Bdikin, I., Gazit, E. & Rosenman, G. Strong piezoelectricity in bioinspired peptide nanotubes. *ACS Nano* **4,** 610–614 (2010).
14. Amit, M. *et al.* Hybrid proton and electron transport in peptide fibrils. *Adv. Funct. Mater.* **24,** 5873–5880 (2014).
15. Berger, O. *et al.* Light-emitting self-assembled peptide nucleic acids exhibit both stacking interactions and Watson–Crick base pairing. *Nat. Nanotechnol.* **10,** 353–360 (2015).
16. del Mercato, L. L. *et al.* Charge transport and intrinsic fluorescence in amyloid-like fibrils. *Proc. Natl Acad. Sci. USA* **104,** 18019–18024 (2007).
17. Amit, M., Cheng, G., Hamley, I. W. & Ashkenasy, N. Conductance of amyloid-based peptide filaments: structure & function relations. *Soft Matter* **8,** 8690–8696 (2012).
18. Creasey, R. C. G., Shingaya, Y. & Nakayama, T. Improved electrical conductance through self-assembly of bioinspired peptides into nanoscale fibers. *Mater. Chem. Phys.* **158,** 52–59 (2015).
19. Domigan, L. J., Healy, J. P., Meade, S. J., Blaikie, R. J. & Gerrard, J. A. Controlling the dimensions of amyloid fibrils: toward homogenous components for bionanotechnology. *Biopolymers* **97,** 123–133 (2012).
20. Herland, A. *et al.* Electroactive luminescent self-assembled bio-organic nanowires: integration of semiconducting oligoelectrolytes within amyloidogenic proteins. *Adv. Mater.* **17,** 1466–1471 (2005).
21. Rizzo, A., Solin, N., Lindgren, L. J., Andersson, M. R. & Inganäs, O. White light with phosphorescent protein fibrils in OLEDs. *Nano Lett.* **10,** 2225–2230 (2010).
22. Bolisetty, S., Adamcik, J., Heier, J. & Mezzenga, R. Amyloid directed synthesis of titanium dioxide nanowires and their applications in hybrid photovoltaic devices. *Adv. Funct. Mater.* **22,** 3424–3428 (2012).
23. Li, C., Adamcik, J. & Mezzenga, R. Biodegradable nanocomposites of amyloid fibrils and graphene with shape-memory and enzyme-sensing properties. *Nat. Nanotechnol.* **7,** 421–427 (2012).
24. Baldwin, A. J. *et al.* Cytochrome display on amyloid fibrils. *J. Am. Chem. Soc.* **128,** 2162–2163 (2006).
25. Saupe, S. J. The [Het-s] prion of *Podospora anserina* and its role in heterokaryon incompatibility. *Semin. Cell Dev. Biol.* **22,** 460–468 (2011).
26. Balguerie, A. *et al.* Domain organization and structure–function relationship of the HET-s prion protein of *Podospora anserina*. *EMBO J.* **22,** 2071–2081 (2003).
27. Wasmer, C. *et al.* Amyloid fibrils of the HET-s(218–289) prion form a β solenoid with a triangular hydrophobic core. *Science* **319,** 1523–1526 (2008).
28. Meyer, J. Iron–sulfur protein folds, iron–sulfur chemistry, and evolution. *J. Biol. Inorg. Chem.* **13,** 157–170 (2008).

29. Solomon, E. I., Sundaram, U. M. & Machonkin, T. E. Multicopper oxidases and oxygenases. *Chem. Rev.* **96,** 2563–2606 (1996).
30. Van Melckebeke, H. *et al.* Atomic-resolution three-dimensional structure of HET-s(218–289) amyloid fibrils by solid-state NMR spectroscopy. *J. Am. Chem. Soc.* **132,** 13765–13775 (2010).
31. Bonisch, H., Schmidt, C. L., Bianco, P. & Ladenstein, R. Ultrahigh-resolution study on *Pyrococcus abyssi* rubredoxin. I. 0.69 A X-ray structure of mutant W4L/R5S. *Acta Cryst. D* **61,** 990–1004 (2005).
32. Page, C. C., Moser, C. C., Chen, X. & Dutton, P. L. Natural engineering principles of electron tunnelling in biological oxidation-reduction. *Nature* **402,** 47–52 (1999).
33. Winkler, J. R. & Gray, H. B. Long-range electron tunneling. *J. Am. Chem. Soc.* **136,** 2930–2939 (2014).
34. Sabaté, R. *et al.* Prion and non-prion amyloids of the HET-s prion forming domain. *J. Mol. Biol.* **370,** 768–783 (2007).
35. Doussineau, T. *et al.* Mass determination of entire amyloid fibrils by using mass spectrometry. *Angew. Chem. Int. Ed.* **55,** 2340–2344 (2016).
36. Siemer, A. *et al.* ^{13}C, ^{15}N resonance assignment of parts of the HET-s prion protein in its amyloid form. *J. Biomol. NMR* **34,** 75–87 (2006).
37. Mizuno, N., Baxa, U. & Steven, A. C. Structural dependence of HET-s amyloid fibril infectivity assessed by cryoelectron microscopy. *Proc. Natl Acad. Sci. USA* **108,** 3252–3257 (2011).
38. Mao, F., Mano, N. & Heller, A. Long tethers binding redox centers to polymer backbones enhance electron transport in enzyme 'wiring' hydrogels. *J. Am. Chem. Soc.* **125,** 4951–4957 (2003).
39. Bard, A. J. & Faulkner, L. R. in *Electrochemical Methods: Fundamentals and Applications* 2nd edn (eds Allen, J. & Bard, L. R. F.) 580 (John Wiley & Sons, 2001).
40. Laviron, E. A multilayer model for the study of space distributed redox modified electrodes. Part I. Description and discussion of the model. *J. Electroanal. Chem. Interfacial Electrochem.* **112,** 1–9 (1980).
41. Blauch, D. N. & Saveant, J. M. Dynamics of electron hopping in assemblies of redox centers. Percolation and diffusion. *J. Am. Chem. Soc.* **114,** 3323–3332 (1992).
42. Andrieux, C. P. & Savéant, J. M. Electron transfer through redox polymer films. *J. Electroanal. Chem. Interfacial Electrochem.* **111,** 377–381 (1980).
43. Barsoukov, E. & Macdonald, J. R. *Impedance Spectroscopy: Theory, Experiment, and Applications* 2nd edn (John Wiley & Sons, 2005).
44. Gabrielli, C., Haas, O. & Takenouti, H. Impedance analysis of electrodes modified with a reversible redox polymer film. *J. Appl. Electrochem.* **17,** 82–90 (1987).
45. Musiani, M. M. Characterization of electroactive polymer layers by electrochemical impedance spectroscopy (EIS). *Electrochim. Acta* **35,** 1665–1670 (1990).
46. Ho, C., Raistrick, I. D. & Huggins, R. A. Application of A-C techniques to the study of lithium diffusion in tungsten trioxide thin films. *J. Electrochem. Soc.* **127,** 343–350 (1980).
47. Bisquert, J., Garcia-Belmonte, G., Bueno, P., Longo, E. & Bulhões, L. O. S. Impedance of constant phase element (CPE)-blocked diffusion in film electrodes. *J. Electroanal. Chem.* **452,** 229–234 (1998).
48. Criado, C., Galán-Montenegro, P., Velásquez, P. & Ramos-Barrado, J. R. Diffusion with general boundary conditions in electrochemical systems. *J. Electroanal. Chem.* **488,** 59–63 (2000).
49. Ordinario, D. D. *et al.* Bulk protonic conductivity in a cephalopod structural protein. *Nat. Chem.* **6,** 596–602 (2014).
50. Malvankar, N. S. *et al.* Tunable metallic-like conductivity in microbial nanowire networks. *Nat. Nanotechnol.* **6,** 573–579 (2011).
51. Rengaraj, S., Kavanagh, P. & Leech, D. A comparison of redox polymer and enzyme co-immobilization on carbon electrodes to provide membrane-less glucose/O_2 enzymatic fuel cells with improved power output and stability. *Biosens. Bioelectron.* **30,** 294–299 (2011).
52. Rubenwolf, S. *et al.* Carbon electrodes for direct electron transfer type laccase cathodes investigated by current density–cathode potential behavior. *Biosens. Bioelectron.* **26,** 841–845 (2010).
53. Feifel, S. C., Kapp, A. & Lisdat, F. Electroactive nanobiomolecular architectures of laccase and cytochrome *c* on electrodes: applying silica nanoparticles as artificial matrix. *Langmuir* **30,** 5363–5367 (2014).
54. Feifel, S. C., Kapp, A., Ludwig, R. & Lisdat, F. Nanobiomolecular multiprotein clusters on electrodes for the formation of a switchable cascadic reaction scheme. *Angew. Chem. Int. Ed.* **53,** 5676–5679 (2014).
55. Winkler, J. R., Gray, H. B., Prytkova, T. R., Kurnikov, I. V. & Beratan, D. N. in *Bioelectronics: From Theory to Applications* (eds Willner, I. & Katz, E.) 15–33 (Wiley-VCH, 2005).
56. Piontek, K., Antorini, M. & Choinowski, T. Crystal structure of a laccase from the fungus *Trametes versicolor* at 1.90-Å resolution containing a full complement of coppers. *J. Biol. Chem.* **277,** 37663–37669 (2002).
57. Le Goff, A., Holzinger, M. & Cosnier, S. Enzymatic biosensors based on SWCNT-conducting polymer electrodes. *Analyst* **136,** 1279–1287 (2011).
58. Holzinger, M., Le Goff, A. & Cosnier, S. Carbon nanotube/enzyme biofuel cells. *Electrochim. Acta* **82,** 179–190 (2012).
59. Daniels, J. S. & Pourmand, N. Label-free impedance biosensors: opportunities and challenges. *Electroanalysis* **19,** 1239–1257 (2007).

Acknowledgements

We thank D. Fenel and G. Schoehn from the IBS/UVHCI platform of the Partnership for Structural Biology in Grenoble (PSB/IBS) for the electron microscopy. We thank S. Saupe for the gift of pET24a(+)-HET-s(218-289)-His_6 and S. Crouzy for his help in building the structural model. AFM measurements were performed on the Commissariat à l'énergie atomique (CEA) Minatec Nanocharacterization Platform (PFNC). The present work was also partially supported by the Labex ARCANE (ANR-11-LABX-0003-01). L.A. and A.R are indebted to CEA for the funding of their PhD fellowships. V.F. and P.R. thank N. Mermilliod and E. Molva, respectively heads of the Transverse Energy and the Nanoscience programs of the CEA, for their scientific and financial support. We thank T. Martin for the careful reading of the manuscript.

Author contributions

C.H., N.D., M.F. and V.F. realized the design of the protein nanowire. C.H., L.A. and N.D. developed the protocol for the chimeric protein production in bacteria and purification. C.H., L.A., C.V., D.M., V.B., N.D. and V.F. performed the biophysical characterization of the bionanowires. S.R., L.A., K.E., C.G., A.L.B.M., A.L.-G., M.H. and N.D. carried out the electrochemical characterization of the bionanowires and L.A., A.R. and P.R. performed the electrical characterizations of the bionanowires. S.R., K.E., A.L.-G. and M.H. designed the electrode functionalized with nanowires and laccase and realized the experiments. M.F., V.B., M.H. and V.F. were responsible for the project management. L.A., S.R., A.L.-G. and V.F. prepared the manuscript. All the authors discussed the results and commented on the manuscript.

Additional information

Supplementary information is available in the online version of the paper. Reprints and permissions information is available online at www.nature.com/reprints. Correspondence and requests for materials should be addressed to M.H. and V.F.

Competing financial interests

The authors declare no competing financial interests.